SPACEBORNE RADAR

Spaceborne remote sensing instruments allow the acquisition of global and synoptic information for Earth Science investigations. In particular, active microwave observations have the added advantage of providing diurnal measurements and are relatively uncontaminated by the intervening atmosphere. Here, we review three different applications of active microwave remote sensing that have contributed geophysical measurements on a scale and accuracy which surpasses what could be accomplished with airborne or in situ observations. These are synthetic aperture radar interferometry, scatterometry and altimetry. For each of these areas, we describe

the measurement principle, the current technology, the applications, and give a brief look into the future.

SPACEBORNE IMAGING RADAR INTERFEROMETRY

Background

Radar interferometry is a technique for combining coherent radar images recorded by antennas at different locations or at different times to form interferograms that permit the detection of small differences in range, to better than the wavelength (λ) of the signal, between the two points of observation. The measurements are extremely useful for construction of high-resolution topographic maps and surface change maps. The observational geometry of across-track interferometry is depicted in Fig. 1. For a given set of repeat-pass observations, from the ith and jth epochs, with baseline B_{ij} and look angle θ, the interferometric phase difference at each sample is

$$\begin{aligned}\Delta\phi_{ij} &= (4\pi/\lambda)B_{ij}\sin(\theta - \alpha_{ij}) + (4\pi/\lambda)\Delta\rho_{ij} \\ &= \phi_{\text{topography}} + \phi_{\text{displacement}}\end{aligned} \tag{1}$$

where α is the tilt of the baseline with respect to the horizontal. The difference in the slant range path length $|\mathbf{r}_i - \mathbf{r}_j|$ is approximated by $\mathbf{B}\cdot\mathbf{r}$. The first term $\phi_{\text{topography}}$ contains phase contributions from the topography of the Earth surface relative to the interferometric baseline. The sensitivity of the measurements to surface relief is directly proportional to the length of the baseline. If the scatterers are displaced by $\Delta\rho_{ij}$ in the range direction between the two observations, then the observed phase will include a second contribution of $(4\pi/\lambda)\Delta\rho_{ij}$ due to this displacement. This additional term $\phi_{\text{displacement}}$ is independent of the spatial baseline. When the ith and jth observations are acquired at the same time (single-pass interferometry), only the first term is relevant. If the ith and jth observations are separated by a time interval, it is generally referred to as repeat-pass interferometry. In the case where more than one observation is available, it is known as multiple-pass interferometry. The reader is referred to the following articles for a more detailed description of the principles of imaging radar interferometry (1,2,3,4).

Here, we consider the more important practical limitations to the solution of Eq. (1) that affect the accuracies of the derived topography or motion field: phase unwrapping; baseline length/orientation; and phase noise. A digital interferogram is the product of two co-registered complex images I_i and I_j^* (* is the complex conjugate). The measured phases are modulo-2π of the absolute phase $\Delta\phi_{ij}$ in Eq. (1). In order to create relative measurements this phase field needs to be unwrapped to remove the 2π ambiguity. This is a difficult task especially if the phase noise (introduced by the radar system) is high or if the phase field has high spatial frequency (2). The unwrapped phase differs from the absolute interferometric phase $\Delta\phi_{ij}$ by an integer number of cycles for the entire phase field. Assuming $\phi_{\text{displacement}} = 0$ in the following discussion, a simple method to determine this constant would be to find one target in the interferogram with known position relative to the interferometer. Other methods for estimating absolute phase have been proposed and are used in different types of processing. Another significant error source results from errors in knowledge of the baseline length and orientation. It is impossible to separate an error in the baseline angle knowledge from a slope in the surface topography. Hence, the sensitivity of interferometer to surface relief is a function of baseline length and orientation. Extremely precise knowledge of the baseline geometry and length is required if absolute height estimates are needed. Phase noise results from various factors including thermal noise, sampling and processing artifacts, and the correlation of individual radar echoes before they are combined to form the interferogram. Uncertainties in baseline orientation cause slowly varying error whereas phase noise (expected to be random) describes the statistical variability of elevation estimates at each sample.

If an interferogram contains a mixture of topography and motion components in the observed phase, additional information is required to separate the two measurements. Much of it depends on the nature and magnitude of the motion field. For example, if a Digital Elevation Model (DEM) of the region of interest is available, then the topographic phase could be removed. On the other hand, multiple interferograms could be used to estimate the two parameters. Some examples in the following sections illustrate several interesting uses of spaceborne interferometric datasets.

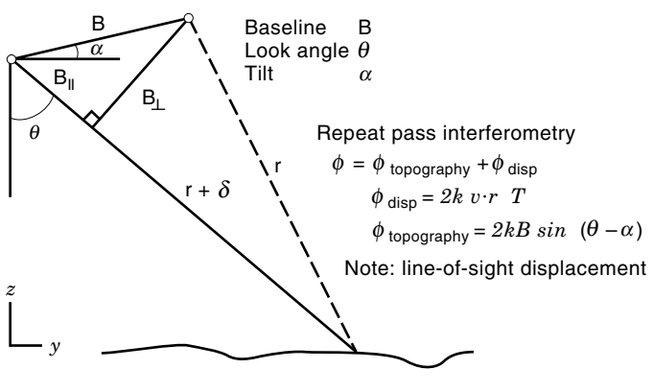

Figure 1. Radar interferometry—imaging geometry.

Evolution of the Technology

Imaging radar interferometry involves a mix of radar technology and data/signal processing techniques. Similar to most application technologies, the rate of development was limited by available datasets for experimentation and verification. Graham (5) of Goodyear Aerospace Corporation first demonstrated the feasibility of operating an airborne imaging radar system in the interferometric mode to generate elevation maps using optically processed data. Their interferometer consists of two antennas mounted one above the other on a side-looking moving gimbal. Subsequently, Zebker and Goldstein (1) at the Jet Propulsion Laboratory (JPL) refined these techniques using digitally processed complex data from a side-looking synthetic aperture radar mounted on the NASA CV990 aircraft. Gray and Ferris-Manning (6) of the Canada Center for Remote Sensing (CCRS) also reported the results of a repeat-track implementation. The single-pass airborne systems of JPL and CCRS have generated extensive datasets for a number of years. Since then, there is a growing number of interferometric systems developed for high resolution topographic mapping and for studies in geology, glaciology, hydrology and forestry. The current JPL TOPSAR sys-

tem has two interferometers, both flush mounted to the fuselage of the DC-8 aircraft and operating at L- and C-bands. The CCRS system uses the C-band channel of radar on the Convair CV-580 aircraft. Other airborne interferometers were developed by the following organizations: Environmental Research Institute of Michigan (7); Norden Systems; and United Technologies. The Technical University of Denmark and Dornier of Germany both have operational airborne interferometers.

Researchers at JPL first demonstrated that interferometric procedures could be applied to satellite SAR data acquired on separate SEASAT passes (2,3). Differential interferometry (using multiple interferograms) was used by Gabriel et al. (8) for detection of subcentimeter surface displacements over a large area. The SEASAT satellite, launched in 1978, provided a key source of satellite data for interferometric studies until the launch of the European Remote Sensing Satellite (ERS-1) in July 1991. The SEASAT SAR was operated at L-band (25 cm wavelength) and the ERS-1 SAR was operated at C-band. Both provided temporal baselines close to three days, but the longer wavelength of SEASAT makes that data less prone to temporal decorrelation. At shorter wavelengths, the data are more prone to temporal decorrelation due to their sensitivity to small-scale changes in the scattering characteristics of the natural medium. The Japanese J-ERS1 radar, launched in 1992, has an L-band SAR, which also provided repeat pass interferometric datasets. The repeat period of 44 days, however, was rather long for certain applications. Numerous Earth science studies have been carried out using these datasets.

The Spaceborne Imaging Radar (SIR-C/X-SAR) missions (both approximately 10 days) were flown in April and October of 1994 and tested the technology of repeat-pass radar interferometry for topographic mapping of the Earth and for detection of surface change. The multifrequency radars mounted in the shuttle bay were operated at L-, C- and X-bands. The L- and C-band radars had vertical and horizontal transmit and receive capabilities for collecting multipolarization observations. These radar datasets allowed an assessment of the relative merits of repeat-pass interferometers for mapping the Earth surface.

During late 1995 and early 1996, the ERS-1 and ERS-2 (launched in 1995) SARs were flown in tandem to collect a near-global dataset suitable for repeat-pass interferometric analysis. The orbits were maintained such that the repeat tracks of the two radars were separated by one day, thus providing 1-day intervals between data acquired for interferometry. Subsequently, ERS-1 was decommissioned as an operational sensor. Late in 1995, the Canadian RADARSAT (another C-band SAR with 24-day repeat) was launched but the orbits were not routinely adjusted to the baseline tolerances required for interferometry. However, it still provided subsets of data suitable for interferometic studies.

These satellite systems have collected significant volumes of repeat-pass datasets. The use of these data for Earth science investigations has grown considerably.

Applications in Earth Science

We provide examples of three Earth Science areas where the use of radar interferometry has blossomed: topographic mapping; measurement of glacial ice motion; and monitoring of earthquakes. The most direct application of radar interferometry is topographic mapping. Accurate DEMs are required by a number of Earth science disciplines including hydrology, ecology, glaciology, geomorphology and atmospheric circulation (9). For example, the JPL/NASA TOPSAR system exhibits errors of about 1 m rms in flatter regions and 3 m in mountainous areas. By comparison, the standard United States Geological Survey (USGS) product generally available has a 30 m posting and a level of accuracy of approximately 7 m. The achievable accuracy is better than standard U.S. maps. For parts of the world that are relatively poorly mapped, topographic mapping using radar interferometry is an alternative to traditional photogrammetric surveys. This is especially attractive in regions where the cloud cover precludes the use of visible sensors.

Goldstein et al. (10) produced the first map of ice motion over the Rutford Ice Stream in Antarctica. In their demonstration, they used an image pair with very small baseline (approx. 4 m) to avoid contamination due to surface relief. The sensitivity to line-of-sight motion is better than 1m/year and comparison of derived measurement with ground-based observations showed good agreement. Subsequently, Joughin et al. (11) and Rignot et al. (12) both demonstrated the observability of ice motion on the Greenland Ice Sheet after the removal of the topographic component of the signal. Kwok and Fahnestock (13) used a sequence of interferograms to separate the motion and topographic components of the measured interferometric phase with the assumption that the motion is constant over the observation period. Other studies have progressed further in the use of interferometric observations to produce maps of grounding lines and multiple observations to derive 3-dimensional velocities. As an illustration, Fig. 2 shows a map of the motion field of the Ross Ice Shelf in Antarctica just east of Roosevelt Island; the topographic component of the phase was removed. Flow patterns east of Roosevelt Island are explained by the flow of ice through the channel bounded by the Shirase Coast (400 to 500 m/year). The situation is more complicated west of Roosevelt Island, where large rifts extend away from the Bay of Whales and slice through the ice shelf. Eventually, these large blocks of ice will separate (an event known as calving) from the shelf ice and flow off as icebergs. Observations such as this have given glaciological investigators an unprecedented view of the velocity fields of the various regimes of glacial ice flow. By analyzing only a few Synthetic Aperture Radar (SAR) images, these interferometric procedures can provide dense fields of observation that otherwise would require many years of extremely expensive fieldwork to compile.

The mapping of coseismic displacement of earthquakes was demonstrated by Massonnet et al. (14,15) and Zebker et al. (16). Massonnet et al. (14) used two images (before and after an earthquake) and removed the topographic component using a simulated topographic phase field generated using an available DEM. Zebker et al. (16) used three complex SAR images: one before and two after the main Landers earthquake in June 1992. The topographic phase is removed by differencing two interferograms—one with surface motion and one without. Again, these techniques have been used routinely to monitor the effects of earthquakes in the past several years. Figure 3 shows a map of ground motion in the aftermath of an earthquake. This figure of the area around Kobe, Japan was created by combining two JERS-1 Synthetic Aper-

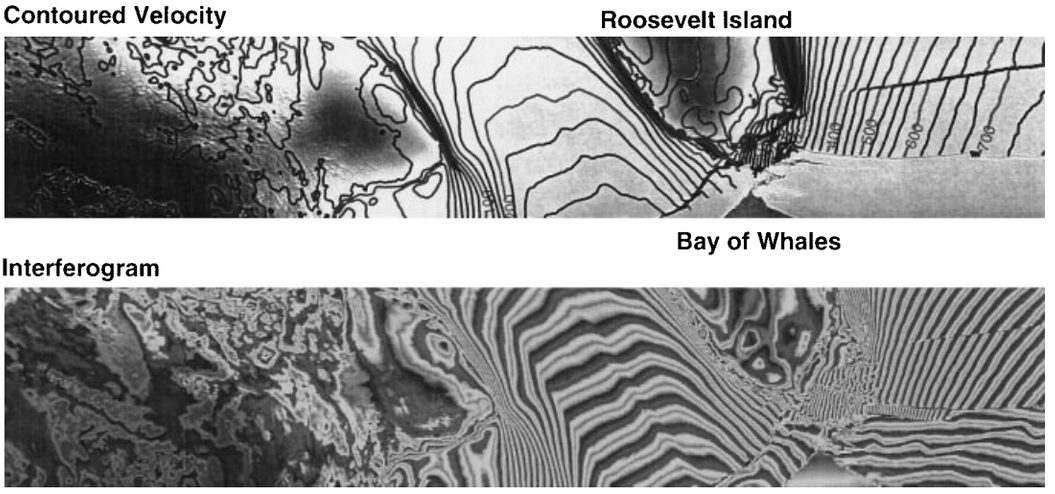

Figure 2. Ice motion of the Ross Ice Shelf, Antarctica near Roosevelt Island. This ERS tandem phase data was recorded at the U.S. McMurdo Reception Facility in Antarctica in January 1996.

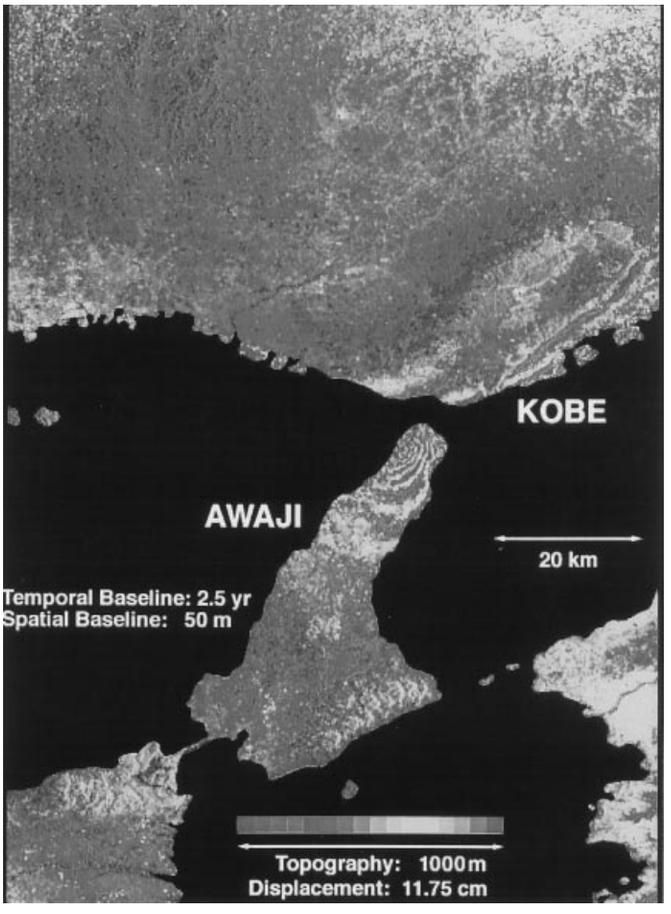

Figure 3. Image showing surface displacement due to the magnitude 7 earthquake in Kobe, Japan derived from JERS-1 data. (Courtesy of Dr. P. Rosen, Jet Propulsion Laboratory, California Institute of Technology.)

ture Radar images acquired two-and-one-half years apart to form an interferogram, which contains a record of the topography of the surface and the change in topography between the imaging times. Because the JERS-1 satellite imaged the area from nearly the same path on orbit (baseline = 0 m at the top of the scene and about 100 m at the bottom of the scene), there is very little sensitivity in the interferogram to the topography: the steep mountains north of the city of Kobe cannot be seen in the color signature of the interferogram. However, the surface changed dramatically over the 2.5 years because the magnitude 7 Kobe earthquake occurred between imaging times. Most of the color variations on Awaji island and in the city of Kobe are the signature of strong displacement of the surface due to the earthquake. The distance that the ground moved is depicted as color contours, with 11.75 cm of distance shown as one cycle of color variation. It can be seen that the ground moved by greater than 1 m from before to after the earthquake. Very noisy colors along the port areas east of Kobe indicate massive surface disruption from liquefaction of the surface and collapse of structures.

Future Perspectives

Radar interferometry is rapidly maturing into a routine tool for providing important measurements for supporting Earth science investigations and other applications. There are a number of spaceborne radar systems on the horizon designed to provide interferometric observations as one of their primary missions.

In 1999, the Shuttle Radar Topography Mission (SRTM) will be launched with the purpose of producing the most accurate and complete topographic map of the Earth surface. The SRTM mission is a joint project of the Department of Defence's National Imagery and Mapping Agency (NIMA), NASA, and the German and Italian Space Agencies. SRTM will build on the technology of the earlier SIR-C/X-SAR missions that were flown in 1994. The objective of the new mission is to collect elevation measurements of nearly 80% of the Earth's land surface. These observations will be assembled

into DEMs. These DEMs will have planimetric resolution of 30 m and a relative height accuracy of 10 m. Maps of this accuracy can be used for a large number of scientific, civilian and military applications. The SRTM interferometer will operate at two frequencies (C- and X-bands). The interferometer will have a baseline of approximately 60 m. A set of antennas will be mounted in the bay of the shuttle and another set will be mounted at the end of a boom deployed from the shuttle bay after orbit insertion. The interferograms are obtained from complex SAR data collected from the two sets of antennas. In this case, we will have a C-band and X-band interferogram for most of the Earth surface. The entire dataset will be acquired in an 11-day mission. The bulk of the data processing to convert the radar signal data to DEMs will take more than a year.

The European Space Agency (ESA) is planning to launch ENVISAT in late 1998 as a followup to the ERS satellites, and the Canadian Space Agency (CSA) is planning the launch of RADARSAT II toward the end of the century. The proposed NASA LightSAR is an imaging satellite that would use advanced technologies to reduce the cost and enhance the quality of images taken with SAR technology. All these spaceborne missions will have an interferometry component. The data from these missions will provide quantitative measurements at an unprecedented spatial and temporal scale into the next century.

SPACEBORNE SCATTEROMETRY: OCEAN WINDS

Background

Wind scatterometers are radars specifically designed to measure wind velocities over the oceans. During the early 1960s, an aircraft radar measurement program conducted by the Naval Research Laboratory indicated that ocean radar clutter was dependent on wind speed and sea state (17,18). Thereafter, NASA sponsored the development of airborne radars with extensive field programs to help interpret scatterometer measurements in terms of oceanic parameters. In 1966, Moore and Pierson (19) proposed a spaceborne scatterometer on a polar-orbiting satellite to obtain ocean surface wind measurements. During the 1970s, NASA sponsored improved aircraft (AAFE RADSCAT) and Skylab-193 scatterometer programs (20,21) that paved the way for a full-blown demonstration of a spaceborne sensor: the SASS experiment.

On June 28, 1978, SASS was launched on SEASAT to provide global measurements of ocean surface wind vectors (22,23). Although SEASAT operated only for three months, SASS demonstrated the feasibility of ocean wind measurements from space. The scientific results can be found in the special issue of *Journal of Geophysical Research* (**88**, No. C3, Feb. 28, 1983).

Following the SASS experiment, the ERS series of satellites with on-board C-band microwave scatterometers (24) have been providing surface wind measurements since 1991. The NASA Scatterometer (NSCAT) aboard the Japanese Advanced Earth Observation Satellite (ADEOS) was launched on August 17, 1996. Although ADEOS-1 ceased operation after June 1997 due to the solar paddle failure, NSCAT has been found to have had a significant impact on numerical weather forecasting, storm monitoring and many other scientific applications. This has prompted NASA to decide to launch a copy of the SeaWinds Scatterometer in early 1999 to fill in the data gap between the NSCAT and ADEOS-2/SeaWinds missions. Subsequent NASA and ESA satellite scatterometers have been planned to extend the time series of satellite wind products to the 21st century.

Measurement Principle

Scatterometers measure ocean surface winds based on the dependence of radar backscatter (σ_o) on ocean surface roughness, which is a function of surface wind velocity. Here, σ_o is defined as the normalized radar cross section of the sea surface. Wind-roughened surfaces in the form of gravity and capillary waves, breaking waves and foam, are due to the balance of wind input and dissipative processes. Changes in wind velocity cause changes in the roughness of these surface waves. Directional response of the ocean surface to wind forcing makes the profiles of gravity and capillary waves rougher in the along-wind direction than those across. Additionally, the nonlinear interaction of long and short ocean waves makes the short ocean waves rougher on the leeward faces of the long waves than on the windward faces (26,27). These surface waves interact with radar waves, and the strength of the returned echoes is modulated by the wind speed and direction.

The typical dependence of microwave ocean backscatter on surface wind velocities is illustrated in Fig. 4. As shown, σ_o is a monotonically increasing function of wind speed at incidence angles above 20°, and has a few decibels (dB) of variation over azimuth angles. σ_o is larger in the upwind direction than in the crosswind direction (upwind-crosswind asymmetry), and there is a small difference between upwind and downwind observations (upwind-downwind asymmetry). These asymmetries are caused by the preferential directional features of surface waves described in the foregoing. At small incidence angles ($<10°$), the backscatter signal is dominated by the specular reflection by the surface, usually referred to as geometric optics scattering. Because the short ocean waves reduce the specular reflectivity of the surface, σ_o has a negative wind speed sensitivity at near normal incidence angles. However, geometric optics scattering is insensitive to wave direction at less than 15° incidence angles. Hence, microwave scatterometers typically operate at above 20° incidence for near-surface wind velocity measurements.

To facilitate the retrieval of surface wind velocities from radar measurements, a geophysical model function (GMF) relating the microwave ocean backscatter to the surface wind velocity is required. In principle, if there is an accurate mathematical representation of ocean surface waves and an accurate scattering theory accounting for the interaction of electromagnetic waves with ocean surfaces, the relationship of σ_o and ocean surface parameters can be established for any observation angles and frequencies. However, present hydrodynamic and electromagnetic theories are not yet mature enough to produce an accurate geophysical model function for operational considerations. An alternative approach for deriving the scatterometer GMF is to empirically correlate the radar measurements with in situ data. A variety of input winds, including numerical weather model winds and buoys, have been considered for the development of such an empirical function (28,29,30). For example, the C-band geophysical model function (30) developed for the European Space

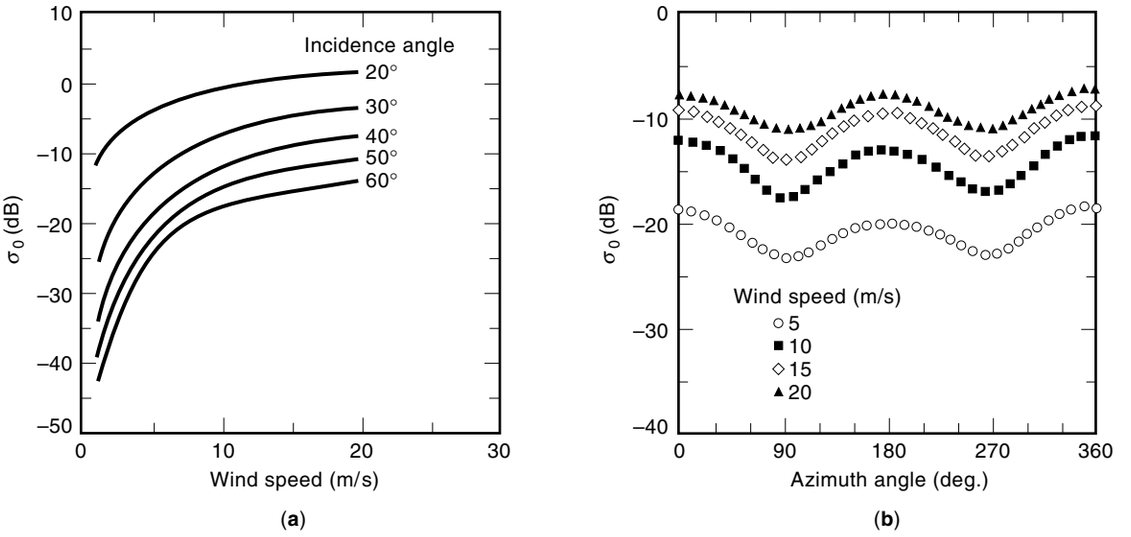

Figure 4. The dependence of microwave ocean backscatter on surface wind velocities at Ku-band derived from NSCAT-1 geophysical model function. 0°, 90°, and 180° azimuth angles correspond to upwind, crosswind, and downwind. Incidence angle is the angle between the direction of surface normal and the radar observation direction.

Agency (ESA) is based on the colocated European Centre for Medium-Range Weather Forecasts (ECMWF) analysis field and ERS-1 scatterometer measurements. A similar approach using the National Center for Environmental Prediction (NCEP) and ECMWF winds together with the Special Sensor Microwave/Imager wind speed products was employed to derive the first version of NSCAT model function (see Fig. 4).

Since σ_0 depends on both wind speed and direction, a single σ_0 measurement is inadequate for the retrieval of both variables (see Fig. 4). To retrieve the wind vector, multiple σ_0 measurements are made at several different azimuthal angles. Figure 5 depicts the measurement geometries of SASS, ERS, NSCAT and SeaWinds scatterometers. SASS collected σ_0 measurements at two azimuth angles separated by 90°, and there are up to four possible wind directions for the

	SASS	NSCAT	SeaWinds	ERS-1/2
Frequency	14.6 GHz	13.995 GHz	13.402 GHz	5.3 GHz
Scan pattern	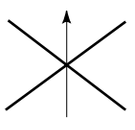	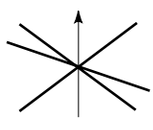	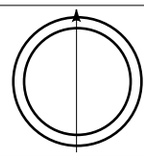	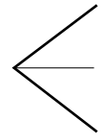
Polarization	V-H, V-H	V, V-H, V	V, H	V only
Beam resolution	Fixed Doppler	Variable Doppler	Spot	Range gate
Resolution	50/100 km	25/50 km	20/25 km	25/50 km
Swath	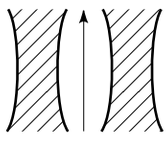	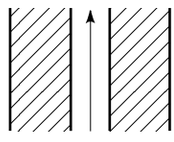	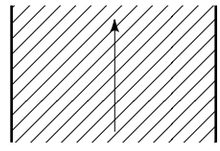	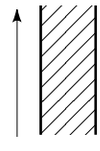
Daily / 2-day coverage	Variable	77/97%	93/100%	41%
Dates	6/78 - 10/78	8/96 - 6/97	11/98 - 11/00 +, 8/00 - 8/03	91 +

Figure 5. Measurement geometries of SASS, ERS scatterometers, NSCAT and SeaWinds.

SASS measurement geometry. To reduce the number of wind direction solutions (ambiguities), ERS scatterometers and NSCAT added one antenna beam to the SASS antenna geometry. Without measurement noise, ERS scatterometers and NSCAT measurements allow unique determination of the correct wind direction. However, the upwind and downwind asymmetry of ocean σ_0 are not significant, and, the correct wind direction (closest to the true) and the one in the opposite direction are often confused by noise. Hence, the ambiguity selection skill, which is defined as the probability that the correct wind direction solution is selected, is a very important parameter for scatterometer performance.

The scatterometer wind accuracy is limited by the accuracies of radar measurements and geophysical model functions. The sources of radar measurement errors result from uncertainties in instrument calibration, background and instrument thermal noise, radar integration time-bandwidth product, and propagation loss through the atmosphere. Instrument calibration errors typically appear as biases and may drift as a function of time. Thermal noise and limited time-bandwidth product uncertainties are expected to be random and are important at low winds because of low signal-to-noise ratio. Atmospheric loss is expected to be smaller for ERS scatterometers operating at C-band (5.3 GHz) than NSCAT operating at Ku-band (13.995 GHz), but will introduce biases in the retrieved wind speed if left uncorrected. In particular, the error caused by atmospheric loss can be significant at high winds typically associated with thick cloud cover and rain. The other major error source for wind retrieval is the uncertainty of the geophysical model function, which may be influenced by many other geophysical parameters besides the winds, such as wave height and sea and air temperatures.

Current Technology

The NSCAT is a follow-on instrument to SASS. It operates at Ku-band and employs antenna fan beams and Doppler filtering to determine the cell resolution. However, based on the study of SASS data, significant improvements have been made to address NASA science requirements. These include the addition of a third antenna beam for each side of the swath and an on-board digital Doppler processor to replace the analog filtering employed by SASS. The detailed design and implementation of each of these subsystems are described in Ref. 31.

The NSCAT antenna subsystem consists of two sets of three antenna fan beams. All NSCAT antenna beams are dual-polarized. The mid-beam can transmit and receive vertical and horizontal polarizations, but NSCAT was designed to excite only the vertical polarization ports of fore and aft antenna beams. The baseline operation scans sequentially through these eight antenna ports in 3.746 s, leading to a sampling resolution of 25 km along the track. The scanning sequence is determined by a beam sequence table containing 8 beam numbers stored in the on-board computer. The addition of a third antenna beam to the SASS design is to improve the ambiguity selection skill of NSCAT. The results of post-launch NSCAT calibration and validation studies have suggested that NSCAT multiple antenna measurements without additional meteorological information allow the selection of the closest solution more than 90% of the time, representing a significant improvement over SASS.

Another improvement of NSCAT over SASS is the use of on-board digital Doppler filtering. Due to the relative motion of spacecraft and Earth surfaces, the Doppler shift of the return echos varies across the swath. The on-board DSS divides the swath into 25 cells based on the Doppler shift. The Doppler center and bandwidth of each of these cells are adjusted as a function of spacecraft orbit location to maintain the swath location and across-track cell resolution. A table containing the constants necessary for the calculation of Doppler frequencies on orbit is called the binning table and is used by the NSCAT on-board computer for real-time calculations. Because the binning and beam sequence tables can be updated and uploadable to the satellite, the along- and across-track resolutions of each NSCAT cell are adjustable. For example, NSCAT has been configured to operate at 6.25 and 12.5 km measurement resolutions for about 2 days during the first three months of operation. The resulting high resolution data have enabled the observations of the significant effects of land surface topography on coastal ocean winds.

SeaWinds is the follow-on to NSCAT. SeaWinds also operates at Ku-band. The SeaWinds system represents a major design change of NASA scatterometers. Instead of using the fan beam design, SeaWinds will use a conically scanning reflector. This is due to the limited space available on ADEOS-2, which does not provide a clear field-of-view for NSCAT-like fan beam antennas with broad elevation antenna beam patterns. As mentioned earlier, the first copy of SeaWinds Scatterometer will go on a U.S. satellite in early 1999. The second copy of SeaWinds will be aboard ADEOS-2 as planned for a year 2000 launch.

The SeaWinds reflector is illuminated by two offset antenna feedhorns, resulting in two spot beams illuminating the Earth surface at 46° and 54° incidence angles. The outer beam operates at vertical polarization and the inner beam operates at horizontal polarization. Because the horizontally polarized ocean backscatter has a larger upwind-downwind asymmetry than the vertically polarized response, the mixed polarization combination was determined to have a better ambiguity selection skill than the other combinations. The antenna reflector is mounted on a spinning assembly with a nominal rotation rate of 18 rpm. The antenna footprints produced by these two antenna beams will trace out two circles on the surface, enabling two to four azimuth radar observations for a given spot on the surface. The relative azimuth angles of these observations vary across the swath, unlike the fan beam designs where the relative azimuth angles are essentially constant from near to far swath. The varying azimuth geometry degrades the measurement performance at outer swath and near nadir track where the fore and aft looks reduce to one or have 180° separation.

Because of the change of antenna design, the signal detection principle and hence the electronics design of SeaWinds is also different from those of NSCAT. The resolution of the SeaWinds radar footprints is basically defined by the size of the antenna reflector and is about 35 km in range and 26 km in azimuth. To improve the range resolution, the SeaWinds radio frequency electronics will chirp the transmit signal over 375 kHz in one pulse length (1.5 m). On-board digital processing will then apply range compression to divide the radar echo into range bins, resulting in about 5 km resolu-

tion in range. This makes the size of the SeaWinds measurement cell comparable to the nominal resolution of NSCAT.

Another important feature of the SeaWinds scanning geometry is that the measurement swath is contiguous without a gap near the subsatellite nadir track, which is present in fan-beam scatterometer designs. Although the accuracy of retrieved wind velocity near the spacecraft nadir track is not as good as that in the mid-swath, a contiguous swath does allow SeaWinds to image 90% of global ice-free oceans in one day compared with two days required for NSCAT.

The ESA has launched two ERS scatterometers since July 1991. ERS scatterometers are part of the Active Microwave Instrument (AMI) on ERS satellites. AMI operating at a frequency of 5.3 GHz (C-band) consists of three operational modes: the image mode; the wave mode, and the wind mode. In the image and wave modes, AMI is configured as a synthetic aperture radar, while in the wind mode, it is configured as a scatterometer. These modes time share the operation in orbit (24).

The ERS scatterometers employ a fan-beam antenna design with three vertically polarized antennas looking to the right-hand side of the satellite. The mid-beam is perpendicular to the ERS-1 ground track and the fore and aft antenna beams are offset by 45° in azimuth with respect to the mid-beam. The antenna beamwidths are 26° in elevation and 0.9° in azimuth for fore and aft beams and 24° in elevation and 1.4° in azimuth for aft beam. These antenna beams provide three radar images of the ocean surface with a swath width of 500 km. However, unlike SASS and NSCAT designs based on Doppler filtering, ERS scatterometers employ short transmit pulses and range gate the return echos to sharpen the resolution along the broad beam direction. This design eliminates the complexity of Doppler filtering, but an on-orbit yaw-steering of ERS satellites was required to compensate for the Doppler shift.

The other distinct feature of ERS scatterometers is the use of high transmit power. Because the traveling wave tube amplifier (TWTA) used for ERS AMI provides an output peak power of 4 kW, the transmit power of ERS scatterometers is much larger than the nominal 100 W output power used by SASS, NSCAT, and SeaWinds. Although 100 W transmit power has been shown to be adequate for fan-beam scatterometers as demonstrated by NSCAT performance, a significantly higher transmit power raises the signal-to-noise ratio (SNR) and reduces the signal detection uncertainties of low wind σ_o at high incidence angles.

The difference in transmit frequencies between ERS and NASA scatterometers leads to several performance differences in geophysical retrieval. The lower operating frequency makes ERS scatterometers less sensitive to atmospheric water vapor and clouds than Ku-band scatterometers; hence C-band scatterometers are expected to outperform Ku-band scatterometers under severe weather conditions. However, C-band backscatter is less sensitive to wind direction, particularly at low winds, and has smaller upwind and downwind backscatter differences. Consequently, Ku-band scatterometers have better wind direction accuracy than C-band scatterometers. It was observed that ERS scatterometers are very inadequate in discriminating the upwind and downwind ambiguities.

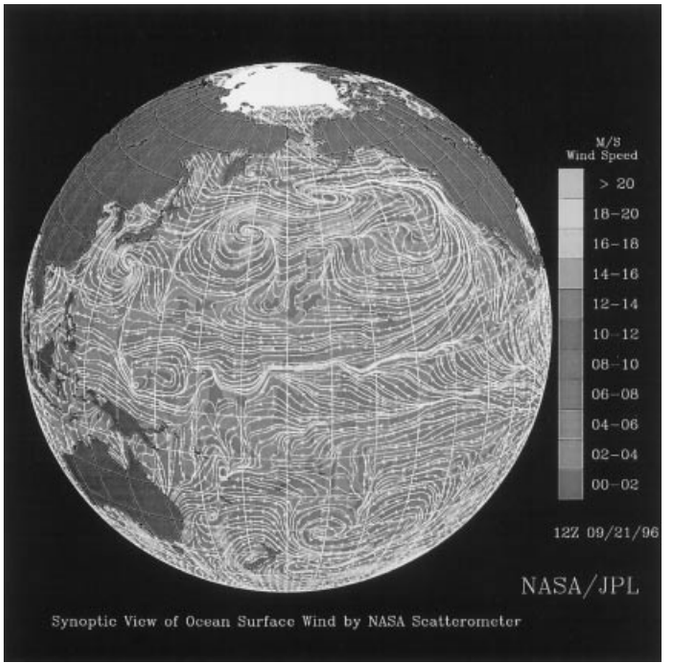

Figure 6. Ocean surface winds provided by NSCAT of the Pacific Ocean on September 21, 1996. The image represents wind speed in meters per second. Dark shading represents low speeds and light shading high speeds. (Courtesy of Drs. W. T. Liu and W. Tang, Jet Propulsion Laboratory, California Institute of Technology.)

Applications in Earth Science

As the largest source of momentum to the upper ocean, winds drive oceanic motions on scales ranging from surface waves to basin-wide current systems. Winds over the ocean modulate air-sea fluxes of heat, moisture, gases, and particulates, regulating the crucial coupling between atmosphere and ocean that establishes and maintains global and regional climates. Figure 6 is an example of global ocean surface winds provided by satellite scatterometers, illustrating the wind velocities over the Pacific Ocean on September 21, 1996, acquired by NSCAT. Gray levels in the image represent wind speed in meters per second. Dark shading shows low speeds and light shading shows high speeds. In the tropical areas just north of the equator, called the Intertropical Convergence Zone, winds from the northern and southern hemisphere collide and force an upwelling of air. In the subtropical areas, air sinks back, creating a zone of divergence and low winds that was long ago called the Horse Latitudes. To the south (north) of the Horse Latitudes in the northern (southern) hemisphere, there are strong, steady winds known as Trade Winds. At latitudes greater than the Horse Latitudes, the Coriolis force is strong. High vorticity in this area creates the cyclones characterizing Earth's weather system. The light spiral features in the upper left near Japan are typhoons Violet and Tom.

Measurement of surface wind velocities can be assimilated into regional and global numerical weather models, thus improving our ability to predict future weather. Satellite wind data, such as those from ERS scatterometers and NSCAT,

have generated more accurate forecasts and extended the useful range of weather forecasts by more than 24 hours in the southern hemisphere. The mapping of wind fields in the equatorial areas of the Pacific Ocean is particular useful for the prediction of El Niño events, leading to changes of rain patterns and weather worldwide. The ability of satellite scatterometers in the prediction of El Niño and other seasonal and annual climate changes will benefit the management of global agriculture, fisheries, and water reserves.

Scatterometer wind data are also valuable for various commerical applications, including storm warning, ship routing, oil production, and marine food harvesting. In a collaborative effort with NASA/JPL, National Oceanic and Atmospheric Administration (NOAA) was able to measure surface winds from NSCAT data within three hours after data acquisition for operational use. The scatterometer data can pinpoint the location, structure, and strength of storms (32), as indicated in Fig. 6. Severe marine storms, including hurricanes near America and typhoons in the western Pacific, are among the most destructive of all natural hazards. The use of satellite scatterometer wind data facilitate the monitoring and forecasting of tropical and mid-latitude storms. Captains of ocean ships can rely on regular scatterometer data with large-scale coverage to choose routes that avoid heavy seas, high head winds, and severe weather systems. As oil production is ongoing at many offshore platforms around the world, long time series of scatterometer wind data will be indispensable for the design of drilling platforms and warnings of impending storms. Because winds drive the ocean currents that transport heat and nutrients, scatterometer data together with other types of spaceborne sensors can be used to study the biogeochemical balance of the ocean-atmosphere system. Detailed wind data from satellite scatterometers can aid in the harvesting of natural seafood crops.

Future Perspectives

As the use of scatterometers becomes more widespread in meteorology, oceanography, and operational weather forecasting, there are several challenges for the development and applications of spaceborne scatterometer technology in the 21st century.

Although satellite scatterometers have already demonstrated a significant impact on climate research and weather forecasting, the volume, mass, and cost of a spaceborne scatterometer mission remains high, creating a significant barrier for these instruments to be flown on operational weather satellites. For instance, the cost of NSCAT and SeaWinds science missions are in the range of 100 to 200 million dollars for a mission life of three years, and both instruments weigh about 300 kg. It is necessary to incorporate new technologies to reduce the size, weight, and power of scatterometers. For example, reducing the noise figure of low-noise amplifiers will enable the reduction of transmit power, hence leading to a smaller demand on spacecraft power. Advanced electronics technology will allow the use of fewer and smaller components, but with more capabilities, resulting in a decrease of size and weight. This in turn will allow the use of a smaller launch vehicle and make it easier to accommodate the instruments on the spacecraft. Furthermore, if the mission lifetime can be extended beyond 3 to 5 years through the use of more reliable components and technologies, spaceborne scatterometry will be more cost-effective.

The temporal coverage and spatial resolution of spaceborne scatterometers need to be improved to enable the study of many natural phenomena with high variability and resolution. The radar footprint size and sampling resolution of ERS scatterometers, NSCAT and SeaWinds are in the range of 25 to 50 km, which is inadequate imaging high resolution features in the weather fronts, wind fields with high vorticity near the eyewall of tropical cyclones, tropical convective cells, and coastal winds. In addition, NSCAT and SeaWinds require a few days to complete coverage of the tropical oceans, where there are significant diurnal-period variations. A more frequent coverage is needed to resolve these variations for investigating tropical air-sea interaction dynamics. These issues will demand a high-resolution scatterometer with an improved swath coverage or a constellation of low-cost instruments.

The main objective of spaceborne scatterometers is to provide surface wind measurements over the global oceans. However, scatterometers also acquire radar measurements over land surfaces and polar sea ice, together occupying more than 30% of the Earth surface. Recent investigations of ERS scatterometers and NSCAT data have indicated that scatterometers have a strong potential for studies of the dynamics and changes of land surface and polar regions, for example, tropical deforestation monitoring, glacier ice sheets, sea ice extent and sea ice motion. The challenge is to come up with an accurate geophysical interpretation of scatterometer data collected over these targets and to develop algorithms for a consistent, quantitative retrieval of geophysical parameters.

ALTIMETRY: LARGE-SCALE OCEAN DYNAMICS

Background

Radar altimetry is used to measure the precise height of sea surface relative to the geocenter, a very useful variable for geophysical studies. Many physical processes affect the height of the sea surface. The dominant factor is the spatially varying gravity field of the Earth, making the sea surface follow the Earth's gravitational equipotential surface, or the geoid. This effect creates a sea surface relief of hundreds of meters. For instance, the height of the Tropical Indian Ocean is lower than that of the western Tropical Pacific Ocean by more than 100 m. The reader is referred to McAdoo and Marks (33) for an example of the applications of altimetry to the study of the Earth's gravity field. Apart from the geoid are sea surface variations of magnitude from centimeters to meters caused by various oceanographic phenomena: tides; waves; currents; storm surges; etc. Among these the effect of currents is most interesting in the study of large-scale ocean dynamics that is key to the understanding of the Earth's climate. The application of altimetry to the measurement of sea surface height for the study of ocean dynamics is the focus of this section.

The fundamental relation between sea surface height and ocean current is the geostrophic balance (34), a balance between the pressure gradient at the sea surface and the Coriolis force resulting from the movement of water on a rotating Earth. The pressure gradient is derived from the ocean topog-

raphy, defined as the elevation of the sea surface relative to the geoid. The ocean topography is directly related to the ocean surface current velocity as follows:

$$u = -\frac{g}{f}\frac{\partial h}{\partial y}$$

$$v = \frac{g}{f}\frac{\partial h}{\partial x}$$

where u is the eastward velocity; v is the northward velocity; x is the east coordinate; y is the north coordinate; h is the elevation of the ocean topography; $f = 2\Omega$ sin (latitude); $\Omega = 7.29 \times 10^{-5}$ s^{-1} (rotation rate of the Earth); and g is the local gravitational acceleration at the sea surface. The velocity determined in this way is not the total surface velocity, but the important component that penetrates the deep ocean. There is a surface boundary layer of directly wind-driven current (called the Ekman layer; see Ref. 34) that has no signatures in ocean topography and hence is invisible to altimeters. This aspect makes altimetry particularly useful for the study of the circulation of the entire water column.

The relief of the global ocean topography is on the order of 1 m, a small signal to retrieve from space. This signal has to be measured with an accuracy of a few centimeters in order to calculate the precise change in the ocean circulation. For instance, a 1 cm tilt of the ocean topography implies the transport of up to several million metric tons of water per second, which is a significant fraction of the transport carried by the major ocean current systems. The challenge of altimetry is to achieve this centimeter accuracy for oceanographic studies.

For a general introduction to altimetry the reader is referred to Stewart (35), Wunsch and Gaposchkin (36), and Chelton et al. (37). The basic concept is straightforward. The radar altimeter bounces microwave pulses from the sea surface and measures the round-trip travel time to determine the altitude of the spacecraft above the sea surface. By subtracting this altitude from the distance between the spacecraft and the geocenter, a distance determined by the technique of precision orbit determination (38), one can thus obtain the height of the sea surface relative to the geocenter.

Shown in Fig. 7 (adapted from Ref. 39) is a schematic representation of the technique of pulse ranging by a radar altimeter. It shows the variation with time of area illuminated by a short, widebeam pulse. The power of the return pulse is proportional to the area of illumination and thus has a similar dependence on time. The time of the arrival of the leading edge of the return pulse is used to determine the range from the sea surface to the radar antenna. In the presence of ocean waves, the wave crests reflect the pulse back to the altimeter sooner than do the wave troughs, creating a further stretch of the leading edge. The extent of the leading edge of the return pulse can thus be used to determine the height of the waves. The frequency used by most radar altimeters is in the range of the Ku band (~14 GHz which corresponds to a wavelength of about 2 cm). At vertical incidence in the case of a radar altimeter, the return signal strength decreases with the amplitude of these centimetric waves, which are extremely sensitive to wind speed. When the wind is weak, the sea surface is smooth and hence reflects more radar signals than a rough sea resulting from a strong wind. A strong return pulse is thus related to low wind speed, and a weak return pulse is related to high wind speed. Therefore, an altimeter can also measure ocean wind speed.

To obtain the centimeter measurement accuracy, a host of technical challenges arises despite the apparent simplicity of the basic measurement principle of radar altimetry. For example, the radar pulse needs to be compressed to resolve travel time in nanoseconds; thousands of pulses need to be transmitted and received every second to average out the noise in the return signals; the delay of electromagnetic waves due to the dry and wet air mass in the troposphere as well as the free electrons in the ionosphere needs to be accounted for; the distance between the center of mass of the spacecraft and the geocenter needs to be determined within a few centimeters (a precision of one in ten millions).

Evolution of the Technology

The early satellite altimeters were primarily flown for proving the concept of this potentially powerful remote sensing tool (40). The noise levels of the altimeters on board Skylab (1974), GEOS-3 (1975–78), and Seasat (1978) were 60, 25, and 10 cm, respectively. The Seasat altimeter (41) was the first to have reached a precision level useful for oceanographic studies. Unfortunately, Seasat lasted only slightly over 100

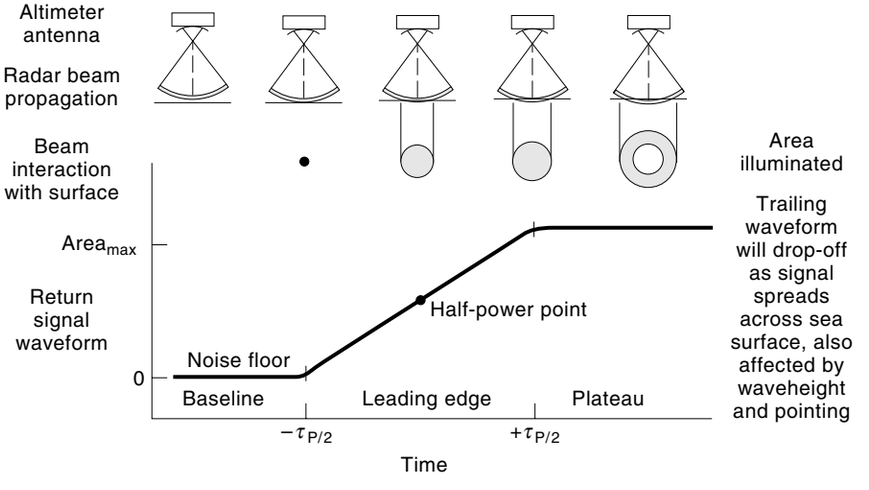

Figure 7. Altimeter pulse interaction with the sea surface and the characteristic return waveform generated by the altimeter electronics [Zieger et al. (38)].

days. The next satellite altimeter was flown by the U.S. Navy's Geosat (1985–89). This instrument has several improvements over the Seasat altimeter (42), notably the longer radar pulse (102.4 μs instead of 3.2 μs). This long pulse, plus some other hardware improvements, has reduced the peak power requirement from 2 kW (for Seasat and GEOS-3) to 20 W, making the instrument more robust. The Geosat altimeter has lasted for four years and generated a rich data set for oceanographic and geophysical studies [the Geosat special issues of the *Journal of Geophysical Research,* **95** (C3,10): 1990 (43)].

Despite the success of Geosat, it has several limitations. The altimeter has only one frequency channel (13.5 GHz) and hence is not able to retrieve the pulse delay caused by the ionospheric free electrons. This delay can create an error of 2 to 20 cm. An altimeter operating at two properly separated frequencies would be able to determine this delay from the difference in pulse travel time between the two signals. The pulse delay by the water vapor in the troposphere creates another source of error of up to 40 cm. This delay requires knowledge of the water vapor content of the atmosphere whose determination would require a microwave radiometer. Such a radiometer was missing in Geosat. Moreover, the uncertainty in the radial position of the Geosat orbit was determined only with an accuracy of 1 m, making the applications to large-scale ocean dynamics difficult.

Launched in August 1992, the United States/France joint TOPEX/POSEIDON Mission (44) has provided a state-of-the-art altimeter system that is specifically designed to meet the challenge posed by the requirement of measuring the large-scale, small signals in sea surface height caused by ocean currents. There are two radar altimeters on board the satellite. The primary one (provided by the United States) operates at two frequencies (13.6 and 5.3 GHz) for retrieving the ionospheric pulse delay. The secondary one (provided by France) is a solid-state, single-frequency (13.65 GHz) system to demonstrate low-power, low-cost technology for future altimeter missions. The primary NASA altimeter has several improvements over the Geosat altimeter (39). The 13.6 GHz channel has a pulse rate of 4000/s compared to Geosat's 1020/s, resulting in reduction of noise level to an rms magnitude of 1.7 cm. The instrument software in waveform sampling and analysis is also improved. The French altimeter, using a different design, performs at a noise level of 2 cm. TOPEX/POSEIDON also carries a three-frequency radiometer for measuring the total columnar water vapor content along the altimeter line-of-sight. This measurement is used to determine the pulse delay caused by the water vapor. The total error in the altimeter range measurement is estimated to be 3.2 cm (rms) at the rate of one measurement per second, covering an along-track distance of 6.2 km.

The precise location of the satellite in orbit is determined by three independent tracking systems (38). Conventional laser tracking was performed by an onboard laser retroreflector array with a worldwide ground network of laser stations. A dual-frequency microwave Doppler system called DORIS (Doppler Orbitography and Radio-positioning Integrated by Satellite) was provided by the French, involving an onboard receiver and a worldwide, densely populated network of ground beacons. An experimental Global Positioning System (GPS) receiver was carried as the third system, which involves the constellation of the GPS satellites and a network of ground stations. The accuracy of the satellite radial orbital position calculated from these measurements with the use of a state-of-the-art model of the Earth's gravity field (45) has reached a level of less than 3 cm. The total uncertainty in the measurement of sea surface height has therefore reached a level of 4 cm, making the signals created by the variability of basin-wide ocean circulation detectable from space for the first time.

Radar altimeters are also part of the payload of the ERS satellite series (46). Single-frequency altimeters were flown on both the ERS-1 (1991 to 1996) and ERS-2 (1995 to the present) satellites. The level of performance of these two altimeters was somewhere between Geosat and TOPEX/POSEIDON. The accuracy of the orbit determination for ERS-2 has been significantly improved by the Precise Range and Range-Rate Equipment (PRARE) system, which failed to work on board ERS-1. However, it has been demonstrated that by adjusting the ERS-1 data to simultaneous TOPEX/POSEIDON data it was possible to minimize the orbit errors in the ERS-1 data (47). A major disadvantage of the ERS system is the lack of a second channel for determining the ionospheric pulse delay.

Applications to Large-Scale Ocean Dynamics

TOPEX/POSEIDON has opened a new door to the study of large-scale ocean circulation and its governing dynamics. A wealth of results can be found in two special issues of the *Journal of Geophysical Research* [**99** (C12): 1994; **100** (C12): 1995], as well as Wunsch and Stammer (48). For the first time scientists can obtain snapshots of the global ocean topography every 10 days and monitor its changes over weeks to years. The ocean is turbulent on a wide range of scales from millimeters to thousands of kilometers, from seconds to years and decades. However, most of the kinetic energy of ocean currents is concentrated at the so-called mesoscales: 100 km in space and 100 days in time. This is the scale of ocean storms, or eddies (49). Figure 8 shows a map of the global distribution of the sea surface variability associated with the ocean eddies. The map was constructed from data taken over one year. It reveals the regions of energetic ocean currents such as the Gulf Stream, the Japan Current (the Kuroshio), the Brazil/Malvinas Current, and the Antarctic Circumpolar Current among others. This type of map is very useful for testing the performance of computer models of ocean circulation (50,51,52), which, when properly calibrated and validated, are powerful tools for studying the Earth's climate system.

Altimetry data are often analyzed in the form of sea surface anomalies, which are deviations of ocean topography from its time-average and represent the variations of ocean currents that are affecting climate variability. Shown in Fig. 9 is a comparison of the sea surface anomalies in the Pacific Ocean derived from the TOPEX/POSEIDON data and the simulation by a state-of-the-art ocean circulation model (52). The degree of similarity is striking, although the amplitude of the anomalies is generally weaker in the model simulation. In December 1994, the 1994–95 El Niño (see Ref. 53 on the subject) reached its peak. Note the manifestation of the El Niño as high (red color) in the central equatorial Pacific in both the data and the model, indicating the capability of the model in simulating major ocean anomalies. However, the quantitative accuracy of the model still needs to be improved.

One effective approach is to apply data assimilation techniques (54) to combining the data with the model such that the information of the sea surface height observation can be used to improve the model simulation of the circulation, as well as temperature and salinity at depths (55,56).

Future Perspectives

The accuracy and precision of the TOPEX/POSEIDON observation has set the standard for future altimetric missions. Since the ocean circulation and its effect on climate has time scales from years to decades and longer, we need to establish a long record of high-quality altimeter data to gain significant understanding of the ocean's role in climate and to improve its prediction. A series of follow-on missions to TOPEX/POSEIDON, called Jason, is currently being developed by France and the United States to extend the TOPEX/POSEIDON-class data record into the 21st century. The first of these series, Jason-1, is planned for launch in 2000. This will be a solid-state, dual-frequency altimeter based on the heritage of the French altimeter on TOPEX/POSEIDON. The satellite will also be equipped with a 3-frequency water-vapor radiometer as well as DORIS, GPS, and laser tracking devices. The objectives are to achieve a performance at the TOPEX/POSEIDON level with a goal of approaching 1 cm accuracy in sea surface height. Some new challenges are to develop new algorithms that would allow: (1) recovery of signals over extremely calm seas or rain cells that produce an impulse-like return waveform; and (2) better determination of the electromagnetic bias (a sea surface height bias towards the ocean wave troughs) that needs to be removed from the data. Another important task is calibration and validation of the system for consistency with TOPEX/POSEIDON to ensure continuity of the data for detecting long-term sea level trends and global change.

There are two other altimetry missions scheduled for the next five years. The U.S. Navy's Geosat Follow-On (GFO), scheduled for launch in 1998, is equipped with a single-frequency altimeter and a two-frequency water-vapor radiometer. Its challenge is to make ionospheric correction using models and data from other sources such as GPS. The ESA's Environment Satellite (ENVISAT), scheduled for launch in 1999, will carry a dual-frequency altimeter and a water-vapor radiometer among several other instruments. The measurement performance will probably be close to that of TOPEX/POSEIDON. However, the satellite will fly in an orbit that is not optimized for large-scale ocean dynamics due to multiple mission objectives.

Given the planned missions noted in the foregoing, the prospects of future altimetric observations are excellent. The bilateral commitment of France and the United States to the continuation of TOPEX/POSEIDON-quality measurement via the Jason series has laid the foundation for a global observing system for monitoring the ocean in the 21st century. The quality promised by the Jason measurements will underlie their utility in serving as a framework to integrate other satellite observations into a powerful data stream for assimilation by sophisticated numerical models. Such a system of data and models will make routine scientific diagnosis and reliable prediction of the ocean and climate changes a reality.

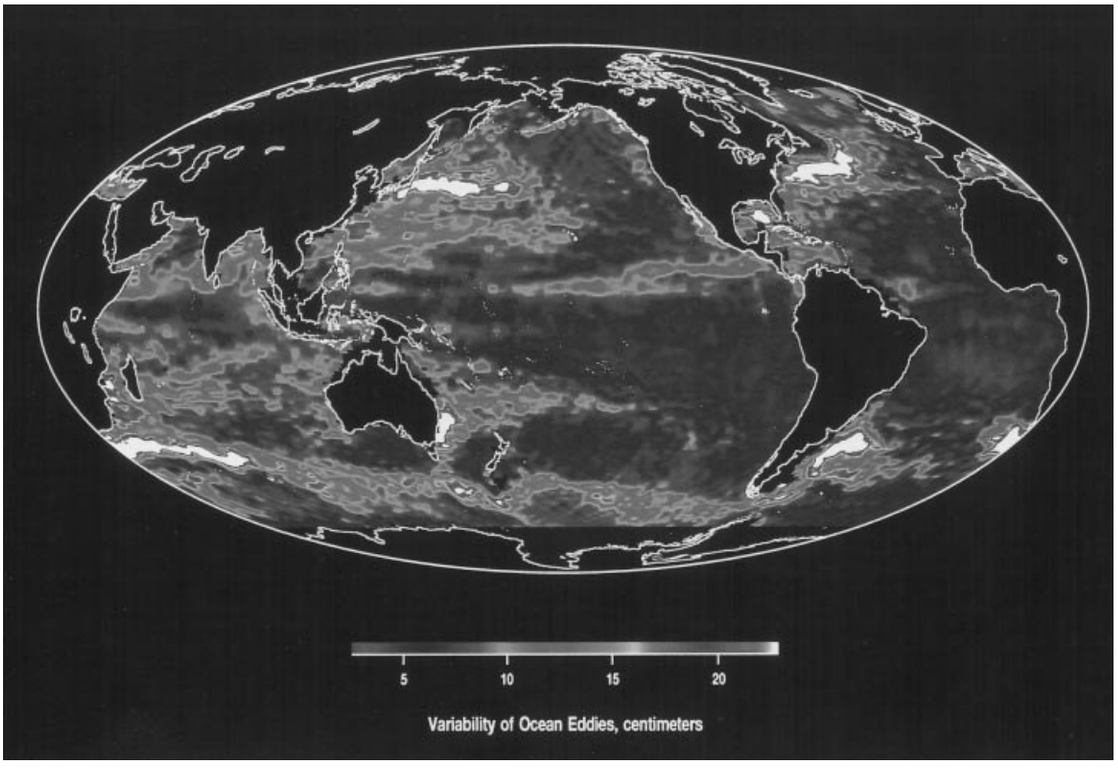

Figure 8. Standard deviation (in centimeters) of the sea surface height variability over the global oceans based on the first year of the TOPEX/POSEIDON data. The white areas represent variabilities larger than 25 cm with peak values larger than 50 cm.

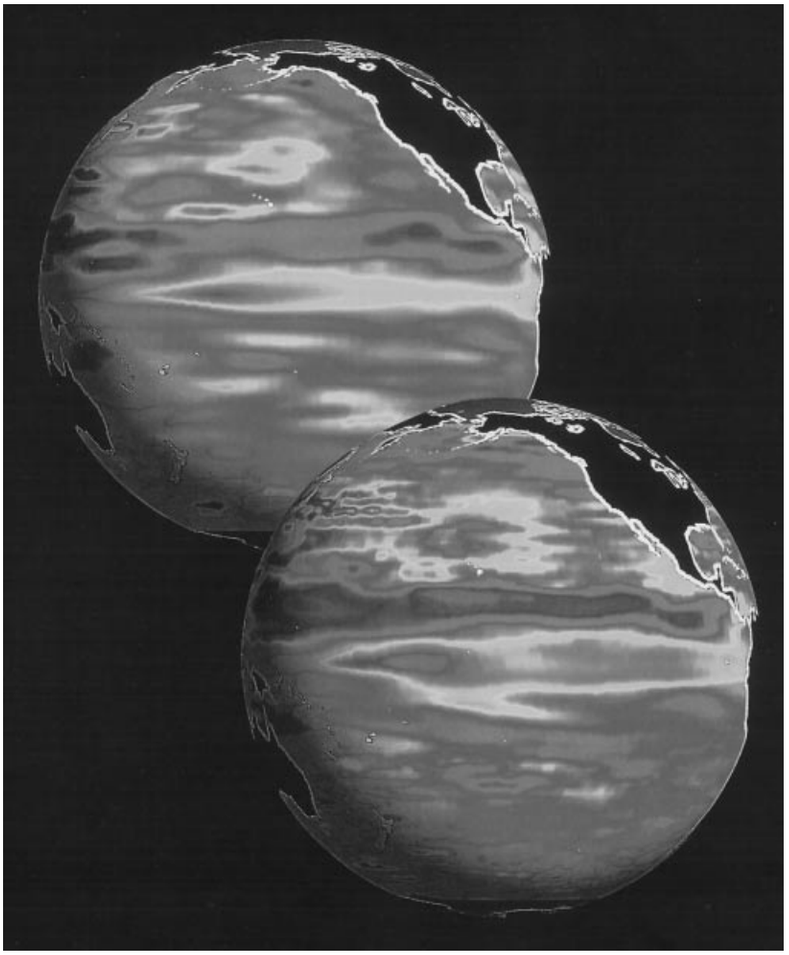

Figure 9. TOPEX/POSEIDON observation (lower) and computer simulation (upper) of the sea level in the Pacific Ocean during December 1994, when the 1994–95 El Niño event reached its peak. The color code shows the sea level relative to a two-year mean averaged over 1993–94. The range of sea level shown is about 30 cm, from −15 cm in magenta to +15 cm in red. The excessive heat associated with the anomalously high sea level in the central equatorial Pacific altered the path of the atmospheric jet stream and caused unusual weather worldwide. [Fu and Smith (52)]

ACKNOWLEDGMENT

This work was carried out by the Jet Propulsion Laboratory, California Institute of Technology, under a contract with the National Aeronautics and Space Administration.

BIBLIOGRAPHY

1. H. A. Zebker and R. Goldstein, Topographic mapping from interferometric SAR observations, *J. Geophys. Res.,* **91** (B5): 4993–4999, 1986.
2. R. M. Goldstein, H. A. Zebker, and C. Werner, Satellite radar interferometry: Two-dimensional phase unwrapping, *Radio Sci.,* **23** (4): 713–720, 1988.
3. F. Li and R. M. Goldstein, Studies of multi-baseline interferometric synthetic aperture radars, *IEEE Trans. Geosci. Remote Sens.,* **28**: 88–97, 1990.
4. E. Rodriguez and J. Martin, Theory and design of interferometric SARs, *Proc. IEE,* **139** (2): 147–159, 1990.
5. L. C. Graham, Synthetic interferometer radar for topographic mapping, *Proc. IEEE,* **62**: 763–768, 1974.
6. A. L. Gray and P. J. Ferris-Manning, Repeat-pass interferometry with airborne synthetic aperture radar, *IEEE Trans. Geosci. Remote Sens.,* **31** (1): 180–191, 1993.
7. H. W. Klimach and G. T. Sos, High performance interferometric SAR description and capabilities, *Proc. of First International Airborne Remote Sensing Conference and Exhibition,* September 11–15, Strasbourg, France, 1994.
8. A. K. Gabriel, R. M. Goldstein, and H. A. Zebker, Mapping small elevation changes over large areas: differential radar interferometry, *J. Geophys. Res.,* **94** (B7): 9183–9191, 1989.
9. D. L. Evans, T. G. Farr, H. A. Zebker, J. J. van Zyl, and P. M. Mouganis-Mark, Radar interferometry studies of the Earth's topography, *EOS Trans. AGU,* **73** (52).
10. R. M. Goldstein, H. Engelhardt, B. Kamb, and R. M. Frolich, Satellite radar interferometry for monitoring ice sheet motion: Application to an Antarctic Ice Stream, *Science,* **262**: 1525–1530, 1993.
11. I. R. Joughin, D. P. Winebrenner, and M. A. Fahnestock, Observations of ice sheet motion in Greenland using satellite radar interferometry. *Geophysical Res. Lett.,* **22** (5): 571-574, 1995.
12. E. Rignot, K. Jezek, and H. Sohn, Ice flow dynamics of Greenland ice sheet from SAR interferometry, *Geophysical Res. Lett.,* **22** (5): 575–578, 1995.
13. R. Kwok and M. A. Fahnestock, Ice sheet motion and topography from radar interferometry, *IEEE Trans. Geosci. Remote Sens.,* **34**: 189–200, 1996.
14. D. Massonnet, M. Rossi, C. Carmona, F. Adraga, G. Peltzer, K. Feigi, and T. Rabaute, The displacement field of the Landers earthquake mapped by radar interferometry, *Nature,* **364**: 138–142, 1993.
15. D. Massonnet, K. Feigi, M. Rossi, and F. Adragna, Radar interferometric mapping of deformation in the year after the Landers earthquake, *Nature,* **369**: 227–230, 1994.

16. H. A. Zebker, P. A. Rosen, R. M. Goldstein, C. Werner, and A. Gabriel, On the derivation of coseismic displacement fields using differential radar interferometry, *J. Geophys. Res.*
17. W. Guinard, J. T. Ransome, Jr., and J. C. Daley, Variation of the NRCS of the sea with increasing roughness, *J. Geophys. Res.,* **76**: 1525, Nov. 1971.
18. C. Daley, Wind dependence of radar sea return, *J. Geophys. Res.,* **78**: 7823–7833, Nov. 1973.
19. K. Moore and W. J. Pierson, Worldwide oceanic wind and wave predictions using a satellite radar-radiometer, *J. Hydronaut.,* **5**: 52–60, 1971.
20. L. Jones, L. C. Schroeder, and J. L. Mitchell, Aircraft measurements of the microwave scattering signature of the ocean, *IEEE J. Oceanic Eng.,* **OE-2**: 52–61, 1977.
21. K. Moore and J. D. Young, Active microwave measurements from space of sea surface wind, *IEEE J. Oceanic Eng.,* **OE-2**: 309–317, 1977.
22. L. Grantham, E. M. Bracalente, W. Linwood Jones, and J. W. Johnson, The SeaSat—A satellite scatterometer, *IEEE J. Oceanic Eng.,* **OE-2**: 200–206, 1977.
23. L. Jones, L. C. Schroeder, D. Boggs, E. M. Bracalente, R. A. Brown, G. J. Dome, W. J. Pierson, and F. J. Wentz, The SEASAT—A satellite scatterometer: The geophysical evaluation of remotely sensed wind vectors over the ocean, *J. Geophys. Res.,* **87** C5: 3297–3317, 1982.
24. E. P. W. Attema, The active microwave instrument on-board the ERS-1 Satellite, *Proc. IEEE,* **79**: 791–799, 1991.
25. L. Tsang, J. A. Kong, and R. T. Shin, *Theory of Microwave Remote Sensing,* New York: Wiley-Interscience, 1985.
26. A. M. Reece, Modulation of short waves by long waves, *Boundary Layer Meteorology,* **13**: 203–214, 1978.
27. A. Donelan and W. J. Pierson, Radar scattering and equilibrium ranges in wind-generated waves with applications to scatterometry, *J. Geophys. Res.,* **92** (C5): 4971–5029, 1987.
28. H. Freilich and R. S. Dunbar, Derivation of satellite wind model functions using operational surface wind analysis: An altimeter example, *J. Geophys. Res.,* **98** (C8): 14,633–14,649, August 15, 1993.
29. C. Rufenach, A new relationship between radar cross section and ocean surface wind speed during ERS-1 scatterometer and buoy measurements, *Int. J. Remote Sensing,* **16** (18): 3629–3647, 1995.
30. A. Stoffelen and D. Anderson, Scatterometer data interpretation—estimation and validation of the transfer function CMOD4, *J. Geophys. Res.,* **102** (C3): 5767–5780, 1997.
31. M. Naderi, M. H. Freilich, and D. G. Long, Spaceborne radar measurement of wind velocity over the ocean—An overview of the NSCAT scatterometer system, *Proc. IEEE,* **79**: 850–866, 1991.
32. W. T. Liu, W. Tang, and R. S. Dunbar, Scatterometer observes extratropical transition of Pacific typhoons, *EOS Trans. AGU,* **78** (23): 237, June 10, 1997.
33. D. C. McAdoo and K. M. Marks, Gravity fields of the Southern Ocean from Geosat data, *J. Geophys. Res.,* **97**: 3247–3260, 1992.
34. J. Pedlosky, *Geophysical Fluid Dynamics,* New York: Springer-Verlag, 1979.
35. R. H. Stewart, *Methods of Satellite Oceanography,* Berkeley, CA: University of California Press, 1985.
36. C. Wunsch and E. M. Gaposchkin, On using satellite altimetry to determine the general circulation of the oceans with application to geoid improvement. *Rev. Geophys. Space Phys.,* **18** (4): 725–745, 1980.
37. D. B. Chelton, E. J. Walsh, and J. L. MacArthur, Pulse compression and sea level tracking in satellite altimetry, *J. Atmos. Oceanic Tech.,* **6**: 407–438, 1989.
38. B. D. Tapley, J. C. Ries, G. W. Davis, R. J. Eanes, B. E. Schutz, C. K. Shum, M. M. Watkins, J. A. Marshall, and R. S. Nerem, B. H. Putney, S. M. Klosko, S. B. Luthcke, D. Pavlis, R. G. Williamson, and N. P. Zelensky, Precision orbit determination for TOPEX/POSEIDON, *J. Geophys. Res.,* **99**: 24383–24404, 1994.
39. A. R. Zieger, D. W. Hancock, G. S. Hayne, and C. L. Purdy, NASA radar altimeter for the TOPEX/POSEIDON Project, *Proc. IEEE,* **79**: 810–826, 1991.
40. L. L. Fu, Recent progress in the application of satellite altimetry to observing the mesoscale variability and general circulation of the oceans, *Rev. Geophys. Space Phys.,* **21:** 1657–1666, 1983.
41. W. F. Townsend, An initial assessment of the performance achieved by the Seasat-1 radar altimeter, *IEEE J. Oceanic Eng.,* **OE-5**: 80–92, 1980.
42. J. L. MacArthur, P. C. Marth, and J. G. Wall, The GEOSAT radar altimeter. Johns Hopkins APL Tech. Digest, **8**: 176–181, 1987.
43. L. L. Fu and R. E. Cheney, Applications of satellite altimetry to ocean circulation studies: 1987–1994, *Rev. Geophys., 32, Supplement,* 213–223, 1995.
44. L. L. Fu, E. J. Christensen, C. Yamarone, M. Lefebvre, Y. Menard, M. Dorrer, and P. Escudier, 1994: TOPEX/POSEIDON Mission Overview, *J. Geophys. Res.,* **99**: 24369–24381, 1994.
45. B. D. Tapley, M. M. Watkins, J. C. Ries, G. W. Davis, R. J. Eanes, S. R. Poole, H. J. Rim, B. E. Schutz, and C. K. Shum, R. S. Nerem, F. J. Lerch, J. A. Marshall, S. M. Klosko, N. K. Pavlis, and R. G. Williamson, The Joint Gravity Model 3, *J. Geophys. Res.,* **101**: 28029–28049, 1996.
46. European Space Agency, ERS-1 Special Issue, *ESA Bulletin,* No. 65, European Space Agency, Paris, 1991.
47. P. Y. Le Traon, P. Gaspar, F. Bouyssel, and H. Makhmaraa, Use of Topex/Poseidon data to enhance ERS-1 data. *J. Atm. Ocean. Tech.,* **12**: 161–170, 1995.
48. C. Wunsch and D. Stammer, Satellite altimetry, the marine geoid and the oceanic general circulation, Ann. Rev. Earth Plan. Sci. (in press).
49. A. R. Robinson, ed., *Eddies in Marine Science,* New York: Springer-Verlag, 1983.
50. A. J. Semtner, Modeling ocean circulation, *Science,* **269**: 1379–1385, 1995.
51. D. Stammer, R. Tokmakian, A. Semtner, and C. Wunsch, How well does a 1/4° global circulation model simulate large-scale oceanic observations? *J. Geophys. Res.,* **101**: 25779–25811, 1996.
52. L. L. Fu and R. D. Smith, Global ocean circulation from satellite altimetry and high- resolution computer simulation, *Bull. Amer. Meteorolog. Soc.,* **77**: 2625–2636, 1996.
53. S. G. Philander, *El Nino, La Nina, and Southern Oscillation,* Boston: Academic Press, 1990.
54. M. Ghil and P. Malanotte-Rizzoli, Data Assimilation in Meteorology and Oceanography, *Adv. Geophys.,* **33**: 141–266, 1991.
55. I. Fukumori, Assimilation of TOPEX sea level measurements with a reduced-gravity, shallow water model of the tropical Pacific Ocean, *J. Geophys. Res.,* **100**: 25027–25039, 1995.
56. D. Stammer and C. Wunsch, The determination of the large-scale circulation of the Pacific Ocean from satellite altimetry using model Green's functions, *J. Geophys. Res.,* **101**: 18409–18423, 1996.

RONALD KWOK
SIMON H. YUEH
LEE-LUENG FU
California Institute of Technology